IJARCCE ISSN (O) 2278-1021, ISSN (P) 2319-5940



International Journal of Advanced Research in Computer and Communication Engineering

Impact Factor 8.471 ⁜ Peer-reviewed & Refereed journal ⁜ Vol. 15, Issue 11, November 2026

DOI: 10.17148/IJARCCE.2026.1511217

A Smartphone and Line-Laser Framework for Tire Tread Depth Estimation: Proposed Design and Validation Protocol

Prajwal N[1], Srikanth[2], Nivedita Nag NVS[3], R Nitish[4], Abhilash L Bhat[5]

Department of Computer Science and Engineering, K S Institute of Technology, Bengaluru, India[1-5]

Abstract: This is a design and protocol paper; it proposes a method and a validation plan and reports no experimental measurements. A single photograph locates tread grooves but cannot give their depth in millimetres, so a metric result needs an extra geometric reference. We therefore propose a smartphone framework with two clearly separated outputs. The measurement mode adds a Class 2 clip-on line laser and a printed ArUco marker and obtains groove depth by triangulating the lateral shift of the laser line, with corrections for phone tilt and for the height difference between the marker plane and the groove floor. The photo-only mode uses the marker solely to normalise image scale and returns a wear category from a specified classifier, never a depth. We derive the measurement model, its resolution and occlusion limits, and a complete error budget: for a 30° laser angle the expanded uncertainty is about 0.05 mm at 1.6 mm depth when the angle is calibrated, but 0.13 mm when a 1° angle error is left uncorrected. We also define a staged validation protocol against a calibrated gauge with acceptance criteria fixed in advance. The legal threshold is a configurable parameter, with the Indian 1.6 mm rule as default.

Keywords: Tread depth, smartphone, line-laser triangulation, ArUco marker, error budget, validation protocol, road safety.

I. INTRODUCTION

Tread grooves drain water from the tyre contact patch, and wet braking distance grows as tread wears and its rubber ages [1]. Wear is gradual, so a tyre can look acceptable long after much of its drainage capacity has gone.

A. Background and Significance

Minimum tread depth is fixed by law. In India, the Central Motor Vehicles Rules require a non-skid depth of at least 1.6 mm for most motor vehicles and 0.8 mm for two- and three-wheelers [2]; other countries use similar limits with different measurement zones, e.g. the United Kingdom [3]. The threshold is therefore a configurable parameter in our framework, with the Indian values as default.

B. Existing Solutions

Owners rely on service checks, coin tests or the moulded wear bars, while gauge readings must be repeated at many points and depend on technique [4]. Workshops and fleets use contact-free optical scanners [5]–[7], and hand-held laser scanners and phone apps are sold commercially [8], [9]. A phone camera alone, however, records groove layout but not depth, so an extra geometric cue is required.

C. Scope and Contributions

No experiments have been carried out yet, and the paper is presented explicitly as a design and validation-protocol paper. Its contributions are:

1) a review of tread-depth techniques organised by the quantity each one senses (Table III);
2) a phone framework that separates a laser-based measurement mode from a photo-only classification mode, with each mode's inputs and outputs fully specified;
3) a measurement model with tilt and floor-height corrections, resolution and occlusion limits, and a worked error budget (Table I);
4) a staged validation protocol with acceptance criteria fixed in advance (Table II).

 This work is licensed under a Creative Commons Attribution 4.0 International License

IJARCCE ISSN (O) 2278-1021, ISSN (P) 2319-5940



International Journal of Advanced Research in Computer and Communication Engineering

Impact Factor 8.471 ⁜ Peer-reviewed & Refereed journal ⁜ Vol. 15, Issue 11, November 2026

DOI: 10.17148/IJARCCE.2026.1511217

II. LITERATURE SURVEY

A. Contact Gauges and Fixed Optical Systems

A pin gauge reads depth at one point, so a tyre survey takes many readings, and the result has long been known to depend on technique [4]; wear bars only show that the limit has been reached. Optical triangulation replaces the pin with a laser: Huang et al. measured tread depth by image triangulation [5], Wang et al. reconstructed the profile of a rotating tyre from a laser plane with errors below 0.2 mm [6], and drive-over stations obtain depth from obliquely imaged light lines [7]. On board, TireEye images the groove cross-section from the wheel well and uses the wear indicators for scale [10]. All of these rely on geometry fixed and calibrated at installation.

B. Hand-held, Smartphone and Depth-Sensor Tools

Hand-held laser scanners such as a palm-size, glove-mounted profiler [8] give dense profiles but are dedicated instruments. Commercial phone apps reconstruct the tread from camera images and quote accuracies around 0.5 mm, but these are vendor figures without independent peer-reviewed validation [9]. Phone depth sensors are another route: the iPhone LiDAR provides only a 256 × 192 depth map and was found reliable for structural vibration at ranges up to about 150 cm [11], and reviews describe it as suited to room- and object-scale scanning [12], far coarser than millimetre grooves. Monocular depth networks predict depth only up to an unknown scale and shift [13].

C. Learning-Based Tyre Assessment

Image-based learning has so far graded rather than measured tread: HOG features with a linear SVM classified tread condition [14], and Mask R-CNN segmented the tread area in phone photographs [15]. Wear has also been predicted indirectly from vehicle and in-tyre acceleration signals [16]. Encoder–decoder segmentation such as U-Net [17] is a candidate for complex tread patterns.

D. Structured Light and Image Processing

A laser line is the simplest structured-light pattern [18]; calibration of the light plane and extraction of the line centre are reviewed in [19]. Edge detection [20], thresholding [21] and contour tracing [22] are available in OpenCV [23].

E. Research Gap and Novelty

Within the literature reviewed, laser triangulation for tread depth is established, so the triangulation principle itself is not claimed as new. What is new is its adaptation to an uncontrolled, hand-held phone: (i) per-capture scale and pose from a printed marker, used to correct tilt and the floor-height scale bias; (ii) an explicit error budget showing which terms dominate; (iii) a strict split between measured and appearance-based outputs; and (iv) acceptance criteria fixed before testing. A dedicated hand-held profiler is likely to be more accurate. The phone approach targets owner-level screening, where its advantages are low accessory cost, a device the user already carries, and a dated history per tyre.

III. METHODS & METHODOLOGY

A. Proposed System

Converting an image to depth requires both scale and depth information. A marker of known size fixes scale, but not depth; a line laser tilted from the camera axis turns height differences into a lateral shift of the line. Two modes follow:

• Mode A (measurement): marker and laser; output is an estimated depth per groove in millimetres and a status from Eq. (13).

• Mode B (photo only): marker only. The marker rectifies the image and resamples it to a fixed 0.05 mm per pixel, so groove width in millimetres and texture features do not depend on shooting distance. Output is a Good, Caution or Replace category from the classifier of Section III-B, item 6; no depth is shown and Eq. (13) is not applied.

B. System Architecture

Fig. 1 shows the processing sequence and Fig. 2 its three layers: acquisition, processing and output. By default, all processing runs on the phone with OpenCV [23], so the app works offline and images never leave the device. The server path in Fig. 2 is optional and opt-in, reserved for a future segmentation model; it is not part of the evaluated design.

 This work is licensed under a Creative Commons Attribution 4.0 International License

IJARCCE ISSN (O) 2278-1021, ISSN (P) 2319-5940

International Journal of Advanced Research in Computer and Communication Engineering

Impact Factor 8.471 ⁜ Peer-reviewed & Refereed journal ⁜ Vol. 15, Issue 11, November 2026

DOI: 10.17148/IJARCCE.2026.1511217



Fig. 1. Processing sequence from capture to result; frames failing the quality check trigger a retake.

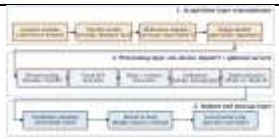


Fig. 2. Layered structure. On-device processing is the default; the server path is optional and opt-in.

1) Hardware and Laser Safety

The clip holds a 650 nm line-laser module of at most 1 mW (Class 2 under IEC 60825-1 [24]) with a 20–25° fan angle, producing a line about 60 mm long and 0.5 mm wide at a 150 mm range, at a nominal angle $\theta = 30°$ to the camera axis. A momentary push button powers the laser only while capturing. The marker is a 40 mm ArUco tag [25] printed on rigid matte card, and an optional 10 nm band-pass filter at 650 nm can be clipped over the lens. Class 2 relies on aversion responses, which are not guaranteed, so the app instructs users never to look into the beam or point it at people, to aim it only down at the tread of a parked vehicle away from traffic, and it disables capture unless the marker is in view.

2) Image Acquisition

The phone is held about 150 mm from the tread, roughly perpendicular to it. Focus and exposure are locked after the first frame, and exposure is kept low enough that the laser line does not saturate. Each capture is a pair of frames taken in quick succession with the laser on and off. Several positions around the tyre are captured, because wear is rarely uniform. A frame is rejected and a retake requested if the variance of its Laplacian falls below a sharpness threshold, its mean brightness is outside a usable band, or the marker is not detected. Fig. 3 shows the capture geometry and Fig. 4 the quantities used below.

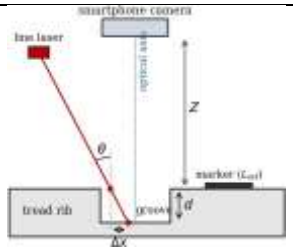


Fig. 3. Mode A geometry: a line tilted by θ meets the rib at x and the groove floor at x + Δx; the marker of side L_{ref} sets the scale.

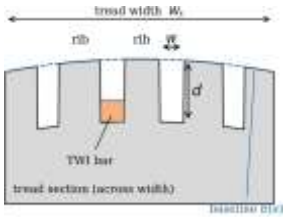


Fig. 4. Tread section with groove width w, depth d, tread width W_t, the wear bar (TWI) and the crown baseline.

3) Preprocessing and Groove Detection

Frames are converted to luminance, smoothed with a Gaussian filter, and contrast-enhanced with CLAHE [26]. Grooves are segmented by an Otsu threshold [21] and a morphological opening with a tall, thin kernel that removes sipes; Canny edges [20] lying on the mask boundary mark the groove walls, and border following [22] yields one contour per groove (Fig. 5). The contours label every column as rib or groove. The rule-based detector assumes circumferential grooves; directional and block patterns require the segmentation network listed as future work. Figs. 5 and 6 use synthetic images: the pipeline has not yet been demonstrated on a real tyre.

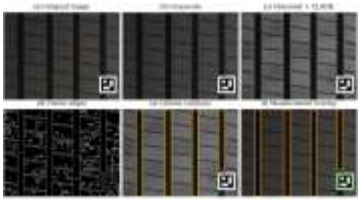


Fig. 5. Pipeline on a synthetic tread (illustration only): (a) input; (b) luminance; (c) CLAHE; (d) Canny edges; (e) groove contours; (f) overlay.

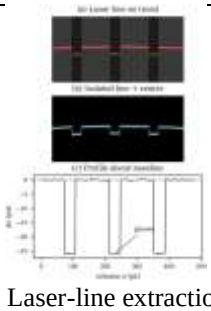


Fig. 6. Laser-line extraction on a synthetic image (illustration only).

 This work is licensed under a Creative Commons Attribution 4.0 International License

IJARCCE ISSN (O) 2278-1021, ISSN (P) 2319-5940

International Journal of Advanced Research in Computer and Communication Engineering

Impact Factor 8.471 ⁜ Peer-reviewed & Refereed journal ⁜ Vol. 15, Issue 11, November 2026

DOI: 10.17148/IJARCCE.2026.1511217

4) Calibration

Once per phone model, Zhang's checkerboard method [27] gives the intrinsic parameters. For each capture, the four marker corners give a homography and, with the intrinsics, the phone pose: range Z and tilt α in the cross-tread plane [28]. Once per clip, θ is calibrated by imaging the line on a machined step of known height and solving Eq. (7) for θ; the target is an uncertainty of 0.2°. Because a refitted clip may change θ, the protocol includes a refit test (Table II).

5) Laser-Line Extraction and Daylight Visibility

Tyre rubber is close to grey, so its red, green and blue values are nearly equal, whereas the 650 nm laser mainly raises the red channel. The chroma image in Eq. (4) therefore suppresses rubber texture and white ambient light, and subtracting the laser-off frame removes the remaining ambient pattern. A rough estimate, still to be measured, shows why this matters: 1 mW spread over a 60 × 0.5 mm line gives about 33 W/m², whereas direct sunlight in a 600–700 nm band delivers roughly 140 W/m², a line-to-background ratio of about 0.2. In shade, or with the 10 nm filter, the ratio rises to about 2. Mode A is therefore specified for shade or the user's own shadow, with or without the filter. Direct-sun performance is tested explicitly (H2) and is not assumed. The line centre in each column is then found by the intensity-weighted centroid of Eq. (5) [19].

6) Reference Baseline, Uneven Wear and Classification

Depth is measured as a gauge does, from the two neighbouring ribs: for each groove, the baseline is the mean line position on the adjacent rib edges, Eq. (6), rather than a single curve across the whole crown. Shoulder wear and cupping therefore affect only the local reference. When the two adjacent rib levels differ by more than 0.3 mm, the result is flagged as uneven wear. Columns where the floor rises abruptly inside a groove are treated as a wear bar and excluded; a bar flush with the ribs triggers Replace directly. Mode A status follows Eq. (13). Mode B uses HOG features [14] of the rectified patch together with groove width in millimetres in a linear SVM. Its training labels come from gauge readings using the same thresholds, and it is evaluated with leave-one-tyre-out cross-validation.

C. Measurement Model

Image positions are written as (u, v), where u runs across the tread. Once the image is rectified, the metric scale on the rib plane follows from the pinhole model [28], as Eqs. (1) and (2) show:

$$s = \frac{L_{\text{ref}}}{\ell_{\text{ref}}} \ [\text{mm/pixel}] \qquad \textbf{(1)}$$

$$s \approx \frac{Z}{f_{\text{px}}} \qquad (2)$$

In these symbols, L_{ref} is the marker's printed side, ℓ_{ref} its rectified side in pixels, and f_{px} the focal length in pixels. The homography H is set by the four marker corners through Eq. (3):

$$\lambda(u', v', 1)^T = H(u, v, 1)^T \qquad \textbf{(3)}$$

The laser stripe is separated from the colour difference between the laser-on and laser-off frames, and its sub-pixel centre in column u is the intensity-weighted mean of Eqs. (4) and (5):

$$I_{\text{r}} = \max(0, C_{\text{on}} - C_{\text{off}}), \quad C = R - \frac{G + B}{2} \qquad \textbf{(4)}$$

$$v_{\text{c}}(u) = \frac{\sum_v v I_{\text{r}}(u, v)}{\sum_v I_{\text{r}}(u, v)} \qquad (5)$$

For a groove g, let $\bar{v}_L$ and $\bar{v}_R$ be the median line positions on its left and right rib edges. The groove baseline is then Eq. (6):

$$b_g = \frac{\bar{v}_{\text{L}} + \bar{v}_{\text{R}}}{2} \qquad \textbf{(6)}$$

A groove depth d shifts the line sideways. Treating phone tilt α as positive when it enlarges the laser incidence angle, the sideways shift measured normal to the camera axis is d sin θ / cos(θ + α), which gives Eq. (7):

 This work is licensed under a Creative Commons Attribution 4.0 International License

IJARCCE ISSN (O) 2278-1021, ISSN (P) 2319-5940



International Journal of Advanced Research in Computer and Communication Engineering

Impact Factor 8.471 ⁜ Peer-reviewed & Refereed journal ⁜ Vol. 15, Issue 11, November 2026

DOI: 10.17148/IJARCCE.2026.1511217

$$d_{\mathrm{A}}(u) = \frac{s\left|v_{\mathrm{c}}(u) - b_g\right| \cos(\theta + \alpha)}{\sin\theta} \qquad \textbf{(7)}$$

If the correction is omitted, the error becomes $-d^2/(Z + d)$. At Z = 150 mm that is about −0.02 mm for a 1.6 mm groove and −0.41 mm for an 8 mm groove. Each groove's depth comes from the median of its central columns, and the tyre value d_{tire} is read from the shallowest groove. Centroid noise δv feeds into depth resolution as Eq. (9) shows:

$$d = \frac{d_{\mathrm{A}} Z}{Z - d_{\mathrm{A}}} \qquad \textbf{(8)}$$

Skipping the correction would leave a bias of $-d^2/(Z + d)$, which is −0.02 mm at 1.6 mm and −0.41 mm at 8 mm for Z = 150 mm. For each groove we take the median over its central columns, and d_{tire} is the smallest of these groove values. A centroid error δv maps to the depth resolution in Eq. (9):

$$\delta d = \frac{s\,\delta v}{\tan\theta} \qquad \textbf{(9)}$$

The laser can light a groove floor of width w only when neither the beam nor the camera's view is cut off by a rib wall. This bounds the deepest groove that can be measured, as Eq. (10) states:

$$d_{\max} = \frac{w}{\tan\theta + \tan|\alpha|} \qquad \textbf{(10)}$$

Plugging in s = 0.05 mm/pixel, δv = 0.5 pixel and θ = 30°, Eq. (9) returns 0.043 mm per column. For a 6 mm groove, Eq. (10) allows 10.4 mm when α = 0 but only 8.0 mm once α reaches 10°. Steeper laser angles sharpen the depth estimate while shrinking the reachable depth range. Assuming the error sources are independent, propagating them through Eqs. (7) and (8) yields the relative variance in Eq. (11):

$$\frac{{\sigma_d}^2}{d^2} \approx \frac{{\sigma_s}^2}{s^2} + \frac{{\sigma_\theta}^2}{\sin\theta^2 \cos\theta^2} + \tan\theta^2\, {\sigma_\alpha}^2 + \frac{s^2 {\sigma_v}^2}{d^2 \tan\theta^2} \qquad \textbf{(11)}$$

Here σ_v lumps together the centroid and baseline uncertainties. When the model is compared against a gauge over N pairs, with error defined as $e_i = \hat{d}_i - d_i$, the 95% limits of agreement are bias ± 1.96σ_e. For the Mode A status decision we use the expanded uncertainty U with coverage factor k = 2. Until validation it is taken from Table I, and afterwards from the measured limits of agreement. Setting $T_c = \max(T_{warn}, T_{min} + U)$, the three-way rule in Eq. (13) is:

$$\mathrm{MAE} = \frac{1}{N}\sum_{i=1}^{N} |e_i|,$$

$$\mathrm{RMSE} = \sqrt{\frac{1}{N}\sum_{i=1}^{N} {e_i}^2}, \qquad \textbf{(12)}$$

$$\mathrm{bias} = \frac{1}{N}\sum_{i=1}^{N} e_i$$

$$\begin{aligned} \mathrm{Status} &= \mathrm{Replace}, \ \text{if } d_{\mathrm{tire}} < T_{\min} \\ \mathrm{Status} &= \mathrm{Caution}, \ \text{if } T_{\min} \le d_{\mathrm{tire}} < T_{\mathrm{c}} \\ \mathrm{Status} &= \mathrm{Good}, \ \text{if } d_{\mathrm{tire}} \ge T_{\mathrm{c}} \end{aligned} \qquad \textbf{(13)}$$

The default T_{min} is 1.6 mm [2]. T_{warn} is an advisory threshold chosen by the user, and the examples use 3 mm.

D. Error Budget

Table I evaluates Eq. (11) for θ = 30°, s = 0.05 mm/pixel and Z = 150 mm. The centroid term assumes a median over 15 columns. All values are model-based, not measured.

 This work is licensed under a Creative Commons Attribution 4.0 International License

IJARCCE ISSN (O) 2278-1021, ISSN (P) 2319-5940

International Journal of Advanced Research in Computer and Communication Engineering

Impact Factor 8.471 ⁜ Peer-reviewed & Refereed journal ⁜ Vol. 15, Issue 11, November 2026

DOI: 10.17148/IJARCCE.2026.1511217

TABLE I ERROR BUDGET FOR MODE A (MODEL-BASED, 1Σ, IN MM)

Source	Assumed 1σ	At d = 1.6 mm	At d = 8.0 mm
Laser angle θ, calibrated	0.2°	0.013	0.064
Laser angle θ, uncalibrated	1.0°	0.064	0.322
Scale s (marker print, flatness)	0.5 %	0.008	0.040
Line centroid (15-column median)	0.16 pixel	0.014	0.014
Rib baseline, Eq. (6)	0.12 pixel	0.010	0.010
Residual tilt after pose correction	0.5°	0.008	0.040
Range Z in Eq. (8)	5 mm	< 0.001	0.014
Expanded U (k = 2), θ calibrated	—	0.05	0.18
Expanded U (k = 2), θ uncalibrated	—	0.13	0.66
Bias if 5° tilt not corrected	—	+0.09	+0.46
Bias if Eq. (8) not applied	—	−0.02	−0.41

Laser-angle error dominates. A 1° error alone produces about a 4% depth error, so the one-time step calibration of θ is essential. Without pose correction, tilt must stay within about ±1° to keep the error below 1%; with correction, ±10° is acceptable for the error budget but reduces d_{max} through Eq. (10). These figures exclude dirt, water and uneven wear, which the protocol measures directly.

E. Validation Protocol

Reference: a digital tread gauge with 0.01 mm resolution and ±0.1 mm or better accuracy, checked against gauge blocks. Its reading is the median of three readings at a chalk-marked point, and the phone is aimed at the same mark (Fig. 7). Stage 1 (pilot): 8 passenger-car tyres (2 new, 3 part-worn, 3 near-limit; two sizes; rib and asymmetric patterns), 4 positions × 3 main grooves = 96 points, 3 captures per point on each of two Android phones (a mid-range and a flagship model, both reported), in indoor diffuse light at Z = 150 mm and $\alpha \approx 0$. This gives 576 captures. Stage 2 (factors, one at a time, 20 tyres): Z = 100, 150 and 200 mm; $\alpha = 0, \pm 5°$ and $\pm 10°$; indoor diffuse light, outdoor shade, direct sun with and without the filter, and low light; clean, dusty and damp surfaces; rib, directional, asymmetric and block patterns. Repeatability uses five captures of one point without handling. Clip reproducibility uses ten remove-and-refit cycles, each with a θ re-check. Hypotheses: (H1) error grows with Z and $|\alpha|$ without pose correction; (H2) the line is not detectable in direct sun without the filter; (H3) grooves deeper than d_{max} are returned as out of range; (H4) Mode B is least accurate near T_{min}. Table II lists the acceptance criteria, which are fixed before any data are collected.

TABLE II ACCEPTANCE CRITERIA FIXED BEFORE TESTING

Metric	Definition	Target
Bias	Mean of e_i, Eq. (12)	$\lvert\text{bias}\rvert \le 0.10$ mm
MAE	Eq. (12), Stage 1	≤ 0.20 mm
95% limits of agreement	bias ± $1.96\sigma_e$	within ±0.40 mm
Repeatability	SD, 5 captures, no handling	≤ 0.10 mm
Clip reproducibility	SD over 10 refits	≤ 0.10 mm
Missed replacement	Points with gauge depth < T_{min} labelled Good	0 (95% upper bound reported)
Mode B	Macro-F1, leave-one-tyre-out	≥ 0.80
Run time	Total per capture, mid-range phone	≤ 1 s

The MAE target is twice the gauge accuracy and one-eighth of the 1.6 mm limit. If the criteria are not met, the results will still be reported in full.

 This work is licensed under a Creative Commons Attribution 4.0 International License

IJARCCE ISSN (O) 2278-1021, ISSN (P) 2319-5940

International Journal of Advanced Research in Computer and Communication Engineering

Impact Factor 8.471 ⁜ Peer-reviewed & Refereed journal ⁜ Vol. 15, Issue 11, November 2026

DOI: 10.17148/IJARCCE.2026.1511217

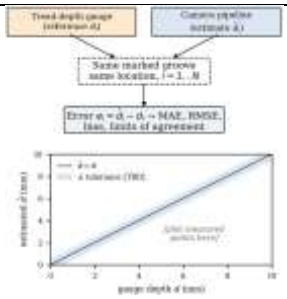


Fig. 7. Validation scheme; the plot is an empty template for Stage 1 data.

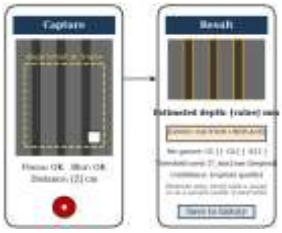


Fig. 8. Planned capture and result screens; bracketed fields are live values.

IV. SYSTEM OUTPUT AND VISUALIZATION

Fig. 8 shows the planned screens. The capture view gives live hints on focus, blur and distance. The result view overlays the detected grooves and lists the depth of each groove, the status, the threshold and jurisdiction used, the uncertainty U and a capture-quality flag. Every result carries a note that it is an estimate, with a gauge check advised near the limit. Mode B results are labelled as visual estimates.

V. RESULTS AND DISCUSSION

No experimental results are reported; this section summarises the analytical results of Section III and compares the design with existing methods.

A. Analytical Results

With θ calibrated to 0.2°, the model predicts U ≈ 0.05 mm near the legal limit and 0.18 mm on a new tyre, within the 0.20 mm MAE target. An uncalibrated 1° angle error raises U to 0.66 mm at 8 mm, so calibration is the critical step. Uncorrected tilt and floor-height effects each bias new-tyre depth by about 0.4 mm, which justifies Eqs. (7) and (8). Wall occlusion caps measurable depth at about 8–10 mm for a 6 mm groove. Daylight visibility, not geometry, is expected to be the main practical risk.

B. Comparison with Existing Methods

Table III compares the design with the methods reviewed in Section II.

TABLE III TREAD-DEPTH ASSESSMENT METHODS COMPARED

Approach	Quantity sensed	Output	Principal drawback
Probe gauge [4]	Pin travel at one point	Depth at one point	Many readings; technique-dependent
Triangulation rig [5], [6]	Laser-line shift	Groove profile, depth	Fixed installation
Drive-over station [7]	Offsets of light lines	Depth across tread	Infrastructure cost
On-board camera [10]	Groove cross-section	Depth while driving	Vehicle integration
Hand-held laser scanner [8]	Laser profile	Dense profile	Dedicated instrument
Phone app [9]	Camera images	Depth (vendor-reported)	No independent validation
Phone LiDAR [11], [12]	Time of flight	Coarse depth map	Too coarse for grooves
Learning on photos [14], [15]	Appearance	Class or mask	No metric depth
This work, Mode A	Laser shift + marker pose	Depth with U	Needs θ calibration; not yet validated
This work, Mode B	Appearance at fixed scale	Category	No metric depth

 This work is licensed under a Creative Commons Attribution 4.0 International License



International Journal of Advanced Research in Computer and Communication Engineering
Impact Factor 8.471 ⁜ Peer-reviewed & Refereed journal ⁜ Vol. 15, Issue 11, November 2026
DOI: 10.17148/IJARCCE.2026.1511217

C. Limitations

A single photograph cannot fix absolute depth [13], so Mode B never reports millimetres. Water, mud or stones in the grooves corrupt detection and depth. In-phone image processing differs between models, so calibrations may not transfer. The output is a screening estimate, not a roadworthiness certificate.

VI. CONCLUSION

This paper sets out a hand-held laser-triangulation design for phones. It keeps millimetre output separate from appearance grading, and its error budget shows that laser-angle calibration, tilt correction and floor-height correction decide whether gauge-level accuracy is achievable. Until the Stage 1 pilot has been carried out, the framework remains a proposal, and it should be judged against the acceptance criteria fixed here.

VII. FUTURE SCOPE

The immediate next step is the Stage 1 pilot. Further work covers a segmentation network [17] for complex treads, automatic θ checks using a printed step target, and a public dataset of tread images paired with gauge readings.

REFERENCES

[1]. A. Genovese et al., "Enhancing wet braking performance: The impact of tire tread material viscoelastic properties and the influence of tread wear," Veh. Syst. Dyn., 2025, doi: 10.1080/00423114.2025.2598002.
[2]. Ministry of Road Transport and Highways, Government of India, The Central Motor Vehicles Rules, 1989, Rule 94(iv), "Condition of tyres," inserted by G.S.R. 221(E), Mar. 28, 2001. [Online]. Available: https://www.indiacode.nic.in
[3]. The Road Vehicles (Construction and Use) Regulations 1986, S.I. 1986/1078, reg. 27(1)(g), United Kingdom. [Online]. Available: https://www.legislation.gov.uk/uksi/1986/1078/regulation/27
[4]. F. C. Brenner and A. Kondo, "Comparative study of tread depth measurement techniques," Tire Sci. Technol., vol. 2, no. 2, pp. 142–156, 1974, doi: 10.2346/1.2167182.
[5]. S.-Y. Huang, Y.-C. Chen, and J.-K. Wang, "Measurement of tire tread depth with image triangulation," in Proc. Int. Symp. Comput., Consum. Control (IS3C), Xi'an, China, 2016, pp. 303–306, doi: 10.1109/IS3C.2016.86.
[6]. X.-B. Wang, A.-J. Li, Q.-P. Ci, M. Shi, T.-L. Jing, and W.-Z. Zhao, "The study on tire tread depth measurement method based on machine vision," Adv. Mech. Eng., vol. 11, no. 4, 2019, doi: 10.1177/1687814019837828.
[7]. V. Uffenkamp, J. Wingbermuehle, G. Nobis, and M. Luther, "Device and method for measuring the tread depth of a tire," U.S. Patent Application 2015/0330773 A1, Nov. 19, 2015.
[8]. D. Boyle and R. H. Tracy, "Palm-size tire tread laser measurement device," U.S. Patent 9 970 748 B2, 2018.
[9]. Anyline GmbH, "Tire Tread Scanner app: What it measures and where it fits," technical note. [Online]. Available: https://anyline.com/news/anyline-tire-tread-scanner-smartphones (accessed Oct. 2026).
[10]. S. Huber, P. Preindl, and J. Betz, "TireEye: Optical on-board tire wear detection," in Proc. Annu. Conf. PHM Soc., vol. 14, no. 1, 2022, doi: 10.36001/phmconf.2022.v14i1.3242.
[11]. G. R. Tondo, C. Riley, and G. Morgenthal, "Characterization of the iPhone LiDAR-based sensing system for vibration measurement and modal analysis," Sensors, vol. 23, no. 18, Art. no. 7832, 2023, doi: 10.3390/s23187832.
[12]. S. F. Abbas and F. M. Abed, "Revolutionizing depth sensing: A review study of Apple LiDAR sensor for as-built scanning applications," J. Eng., vol. 30, no. 4, 2024, doi: 10.31026/j.eng.2024.04.11.
[13]. R. Ranftl, K. Lasinger, D. Hafner, K. Schindler, and V. Koltun, "Towards robust monocular depth estimation: Mixing datasets for zero-shot cross-dataset transfer," IEEE Trans. Pattern Anal. Mach. Intell., vol. 44, no. 3, pp. 1623–1637, Mar. 2022, doi: 10.1109/TPAMI.2020.3019967.
[14]. E. Petrović, D. Ristić-Durrant, M. Simonović, Ž. Ćojbašić, and V. Nikolić, "Vision-based inspection of tyre tread depth," Trans. FAMENA, vol. 45, no. 3, pp. 19–28, 2021, doi: 10.21278/TOF.453024420.
[15]. E. Petrović, M. Simonović, D. Dimitrijević Jovanović, L. V. Dimitrov, and V. Nikolić, "Deep learning-based instance segmentation for detection of tire tread area," Prog. Eng. Sci., vol. 2, no. 2, Art. no. 100080, 2025, doi: 10.1016/j.pes.2025.100080.
[16]. K. Kim, H. Park, and T. Kim, "Comparison of performance of predicting the wear amount of tire tread depending on sensing information," Sensors, vol. 23, no. 1, Art. no. 459, 2023, doi: 10.3390/s23010459.
[17]. O. Ronneberger, P. Fischer, and T. Brox, "U-Net: Convolutional networks for biomedical image segmentation," in Proc. Med. Image Comput. Comput.-Assist. Interv. (MICCAI), LNCS vol. 9351, 2015, pp. 234–241, doi: 10.1007/978-3-319-24574-4_28.
[18]. A. K. C. Wong, P. Niu, and X. He, "Fast acquisition of dense depth data by a new structured light scheme," Comput. Vis. Image Underst., vol. 98, no. 3, pp. 398–422, Jun. 2005, doi: 10.1016/j.cviu.2004.09.003.

 This work is licensed under a Creative Commons Attribution 4.0 International License



International Journal of Advanced Research in Computer and Communication Engineering
Impact Factor 8.471 ⁜ Peer-reviewed & Refereed journal ⁜ Vol. 15, Issue 11, November 2026
DOI: 10.17148/IJARCCE.2026.1511217

[19]. X. Xu, Z. Fei, J. Yang, Z. Tan, and M. Luo, "Line structured light calibration method and centerline extraction: A review," Results Phys., vol. 19, Art. no. 103637, 2020, doi: 10.1016/j.rinp.2020.103637.
[20]. J. Canny, "A computational approach to edge detection," IEEE Trans. Pattern Anal. Mach. Intell., vol. PAMI-8, no. 6, pp. 679–698, Nov. 1986, doi: 10.1109/TPAMI.1986.4767851.
[21]. N. Otsu, "A threshold selection method from gray-level histograms," IEEE Trans. Syst., Man, Cybern., vol. SMC-9, no. 1, pp. 62–66, Jan. 1979, doi: 10.1109/TSMC.1979.4310076.
[22]. S. Suzuki and K. Abe, "Topological structural analysis of digitized binary images by border following," Comput. Vis., Graph., Image Process., vol. 30, no. 1, pp. 32–46, 1985, doi: 10.1016/0734-189X(85)90016-7.
[23]. G. Bradski, "The OpenCV library," Dr. Dobb's J. Softw. Tools, vol. 25, no. 11, pp. 120–125, Nov. 2000.
[24]. Safety of Laser Products—Part 1: Equipment Classification and Requirements, IEC Standard 60825-1:2014, International Electrotechnical Commission, Geneva, 2014.
[25]. S. Garrido-Jurado, R. Muñoz-Salinas, F. J. Madrid-Cuevas, and M. J. Marín-Jiménez, "Automatic generation and detection of highly reliable fiducial markers under occlusion," Pattern Recognit., vol. 47, no. 6, pp. 2280–2292, 2014, doi: 10.1016/j.patcog.2014.01.005.
[26]. K. Zuiderveld, "Contrast limited adaptive histogram equalization," in Graphics Gems IV, P. S. Heckbert, Ed. San Diego, CA, USA: Academic Press, 1994, pp. 474–485.
[27]. Z. Zhang, "A flexible new technique for camera calibration," IEEE Trans. Pattern Anal. Mach. Intell., vol. 22, no. 11, pp. 1330–1334, Nov. 2000, doi: 10.1109/34.888718.
[28]. R. Hartley and A. Zisserman, Multiple View Geometry in Computer Vision, 2nd ed. Cambridge, U.K.: Cambridge Univ. Press, 2004.

 This work is licensed under a Creative Commons Attribution 4.0 International License